Shin et al. *NPG Asia Materials* (2023) 15:10
https://doi.org/10.1038/s41427-023-00467-y

NPG Asia Materials

ARTICLE Open Access

Direct correlation between spin states and magnetic torques in a room-temperature van der Waals antiferromagnet

Hyun Jun Shin[1], Jin Seok Kim[1], Jong Hyuk Kim[1], Jae Yeon Seo[1], Jae Min Hong[1], Ki Won Jeong[1], Kyungsun Moon[1], Mi Kyung Kim[1], Nara Lee[1] and Young Jai Choi[1]

Abstract

Explorations of van der Waals (vdW) antiferromagnets have revealed new avenues for understanding the fundamentals of highly anisotropic magnetism and realizing spin-based functional properties. However, there is a serious limitation to the feasibility of spintronic applications at room temperature owing to the lack of suitable materials. In this work, we examined the anisotropic magnetic characteristics of Co-doped Fe_5GeTe_2, a high-T_N antiferromagnet with $T_N = 350$ K in which magnetic multilayers are intrinsically formed. Our spin-model calculations with uniaxial anisotropy quantify the magnetocrystalline anisotropy energy and visualize the specific spin arrangements varying in the presence of rotating magnetic fields at room temperature. We further show that the spin configurations can be profoundly relevant to the distinctive evolution of magnetic torques in different magnetic phases. Our advanced approach offers a high-T_N vdW antiferromagnet as a magnetic platform to establish room-temperature spin-processing functionalities.

Introduction

Magnetic van der Waals (vdW) materials form intrinsic magnetic multilayers with two-dimensional (2D) crystal structures, acting as an ideal platform for the investigation of fundamental low-dimensional magnetism. They interestingly offer favorable circumstances to implement spintronic applications[1–8]. In contrast to 3D magnetic materials, interlayer spin interactions in 2D magnets alone cannot stabilize a long-range magnetic order at finite temperatures[9]. Magnetocrystalline anisotropy is essential to establish a long-range spin order stable against the inevitable thermal fluctuations in 2D magnetic systems[10–13]. A vdW gap assists the development of indirect exchange coupling between 2D magnetic layers, which determines the type of magnetic ground states and leads to highly anisotropic magnetic properties. In addition, 2D vdW materials with assorted elements crystallized in various structures are expected to exhibit a wide variation in the magnetocrystalline anisotropy, which is crucial in fabricating a variety of magnetic orders and magnetic field-induced phases[14–18].

The intrinsic magnetocrystalline anisotropy resulting from a sizable spin-orbit coupling is determined partially by the crystal structure of magnetic materials. A good example exhibiting the effect of magnetocrystalline anisotropy on the magnetic order is a spin-flop transition[19–21]. A spin-flop transition often induces a significant change in the anisotropic electromagnetic properties of the material through phase conversion. A controlled anisotropic phenomenon offers an in-depth understanding of the fundamental magnetism and broad spintronic applicability[22–25].

Fe_5GeTe_2, an iron-based vdW itinerant ferromagnet with a high Curie temperature ($T_C \approx 310$ K), crystallizes in a rhombohedral structure ($R\bar{3}m$ space group)[26]. However, substantial Co doping, i.e., $(Fe_{1-x}Co_x)_5GeTe_2$, leads to

Correspondence: Mi Kyung Kim (kkummi.mi@yonsei.ac.kr) or
Nara Lee (eland@yonsei.ac.kr) or Young Jai Choi (phylove@yonsei.ac.kr)
[1]Department of Physics, Yonsei University, Seoul 03722, Korea
These authors contributed equally: Hyun Jun Shin, Jin Seok Kim

© The Author(s) 2023
Open Access This article is licensed under a Creative Commons Attribution 4.0 International License, which permits use, sharing, adaptation, distribution and reproduction in any medium or format, as long as you give appropriate credit to the original author(s) and the source, provide a link to the Creative Commons license, and indicate if changes were made. The images or other third party material in this article are included in the article's Creative Commons license, unless indicated otherwise in a credit line to the material. If material is not included in the article's Creative Commons license and your intended use is not permitted by statutory regulation or exceeds the permitted use, you will need to obtain permission directly from the copyright holder. To view a copy of this license, visit http://creativecommons.org/licenses/by/4.0/.

modulation of the interlayer magnetic interactions and magnetocrystalline anisotropy. For $0.4 < x < 0.5$, the crystal structure of this material is altered to another rhombohedral phase ($P\overline{3}m1$ space group) with an A-type antiferromagnetic (AFM) order[27,28]. Interestingly, despite the changes induced in its magnetic order type and structure by chemical doping, the high critical T_C is maintained. At a proper Co doping ratio, the A-type AFM spin configuration exhibits the spin-flop transition for a certain magnetic field strength. It has been shown that $(Fe_{1-x}Co_x)_5GeTe_2$ regains its ferromagnetic phase for $x \geq 0.5$, with $T_C \approx 310$ K and a polar hexagonal structure ($P6_3mc$ space group)[29].

In contrast to ferromagnets, the study of the anisotropic properties in antiferromagnets, including their various origins and controllable factors, has not been considerably performed. In this study, we explored the magnetic anisotropy in the high-temperature vdW antiferromagnet $(Fe_{0.54}Co_{0.46})_5GeTe_2$ (FCGT) using magnetic torque measurements. We determined the magnitude of its magnetocrystalline anisotropy energy and visualized the detailed spin configurations that evolved with the application and rotation of a magnetic field using the microscopic spin model with easy-axis magnetocrystalline anisotropy. Furthermore, we demonstrated that the verified spin states are directly related to distinctive magnetic phases characterized by progressive reversal of the angle-dependent torque across the spin-flop transition. Our proposed approach provides useful guidance for the analysis of the intricate magnetic characteristics of FCGT, which can be extended to other vdW antiferromagnetic materials.

Materials and methods

Sample preparation

To obtain FCGT single crystals, we utilized the isothermal chemical vapor transport method with an iodine agent. We mixed powder or granule forms of Fe, Co, Ge, and Te in an excess molar ratio of Fe and Co with 2 mg/cm^3 iodine and sealed the mixture in an evacuated quartz tube. The quartz ampoule was placed in a muffle furnace at 750 °C for 2 weeks for crystallization. Then, it was quenched in ice water to exclude the accidental formation of high-temperature phases. The iodine remaining on the surface of the crystals was washed off by ethanol.

Magnetization and magnetic torque measurements

The magnetic susceptibility and isothermal magnetization were measured in the T range from 2 to 400 K and H range from −9 to 9 T using a vibrating sample magnetometer (VSM) module in a physical properties measurement system (PPMS, Quantum Design, Inc.). The magnetic torque measurement was carried out utilizing the torque magnetometer option in the PPMS. A single crystal was mounted on a piezoresistive cantilever attached to the torque magnetometer chip (P109A, Quantum Design, Inc.). A Wheatstone bridge circuit was adopted to detect subtle variations in the magnetic torque (1×10^{-9} N·m) through the resistance change.

Uniaxial anisotropic spin model

The spin Hamiltonian with uniaxial magnetocrystalline anisotropy can be expressed as

$$\mathcal{H}/N = J\sum_{i=1}^{2}\vec{S}_i \cdot \vec{S}_{i+1} - g\mu_B\vec{H}\cdot\sum_{i=1}^{2}\vec{S}_i + K\sum_{i=1}^{2}\sin\theta_i,$$

where N denotes the number of Fe/Co moments in a single layer. The first term represents the AFM interactions, in which J designates the AFM coupling strength ($J > 0$) between Fe/Co moments in two neighboring layers. The second term corresponds to the Zeeman energy, in which the magnetic field lies on the plane perpendicular to the [110] direction and deviates from the c-axis by an angle θ, with $g = 2$. The third term represents the easy c-axis magnetocrystalline anisotropy energy, where K denotes the magnetocrystalline anisotropy constant. Fitting the theoretical results of anisotropic magnetization to the experimental data leads to the parameters J and K: $g\mu_B H_{\mathrm{flop}}S/JS^2 = 1.75$ and $K = 0.36JS^2$ for $T = 2$ K and $g\mu_B H_{\mathrm{flop}}S/JS^2 = 1.08$ and $K = 0.16JS^2$ for $T = 300$ K.

Results

Measured and calculated anisotropic magnetization

FCGT crystallizes in a rhombohedral structure ($P\overline{3}m1$ space group) with lattice constants $a = b = 0.4023$ nm and $c = 0.9811$ nm (Supplementary S1). As shown in Fig. 1a, magnetic Fe/Co layers are separated by vdW gaps. Fe/Co 1 sites are half-filled, whereas Fe/Co 2 and 3 sites are fully occupied (Table S1 in Supplementary Information). The relative ratio between Fe and Co atoms was identified by electron probe microanalysis (Table S2 in Supplementary Information). The high-temperature (T) AFM order with $T_N = 350$ K was determined by an anomaly in the magnetic susceptibility, $\chi = M/H$, measured up to 400 K under $H = 0.05$ T upon warming after zero-field (H) cooling (Fig. 1b). The different χ curves for H_c ($H//c$) and H_{ab} ($H\perp c$) reveal the highly anisotropic character for temperatures below T_N. The faster decay of χ below T_N for H_c indicates that the magnetic moments of Co/Fe ions are aligned along this axis. This is consistent with the A-type AFM order in which the net magnetic moments for the adjacent two layers are arranged oppositely to the c-axis, as depicted in the schematic of Fig. 1a.

The highly anisotropic characteristic of the magnetic properties is elucidated in isothermal magnetization (M) data, as shown in Fig. 1c, e. The linear increase in M_c (M for H_c) in the low H_c regime at 2 K indicates a fractional

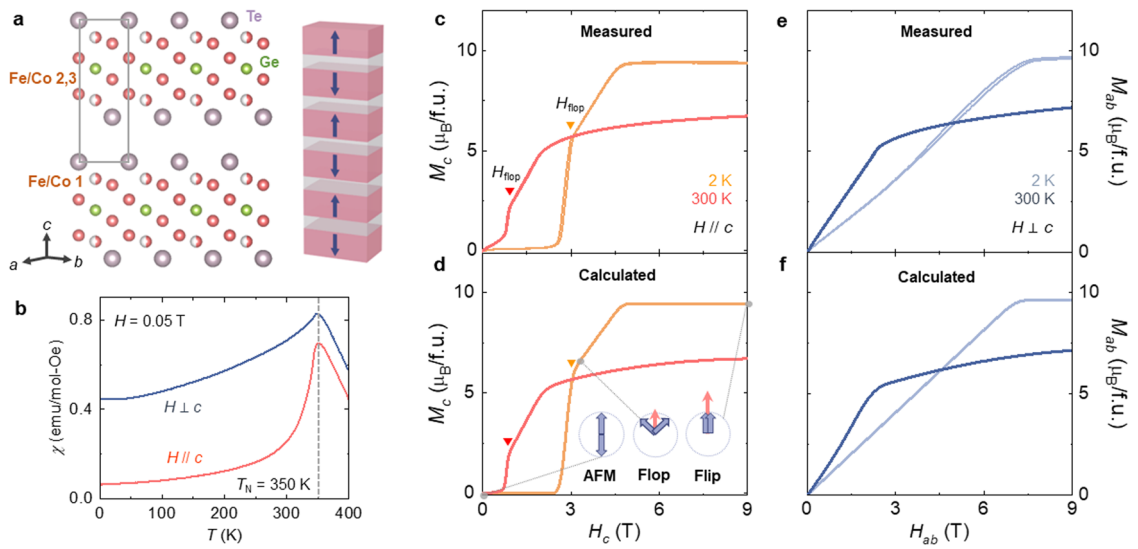

Fig. 1 High-T_N antiferromagnetism of $(Fe_{0.54}Co_{0.46})_5GeTe_2$ (FCGT). a Crystallographic structure of FCGT viewed along the [110] direction. The red, green, and light purple spheres indicate Fe/Co, Ge, and Te atoms, respectively. Fe/Co 1 sites are half-filled, whereas Fe/Co 2 and 3 sites are fully occupied. The gray rectangle designates a unit cell. The schematic depicts the formation of a multilayered magnetic structure, i.e., A-type antiferromagnetic order. **b** Magnetic susceptibility, $\chi = M/H$, measured upon warming under $H = 0.05$ T after zero-field cooling for $H//c$ and $H\perp c$. The vertical dashed gray line specifies the Néel temperature, $T_N = 350$ K. **c** Isothermal magnetization measured for $H//c$ (M_c) at $T = 2$ and 300 K. The red and orange inverted triangles denote the occurrence of spin-flop transitions, $H_{flop} = 2.8$ and 0.8 T for $T = 2$ and 300 K, respectively. **d** Calculated M_c for $T = 2$ and 300 K, estimated from a uniaxial anisotropic spin model. The schematics illustrate the angles of the magnetic moments (blue arrows) for the AFM, spin-flop, and spin-flip states at $T = 2$ K. The red arrows correspond to the strength of H_c. **e** Isothermal magnetization measured for $H\perp c$ (M_{ab}) at $T = 2$ and 300 K. **f** Calculated M_{ab} for $T = 2$ and 300 K.

flip of Fe/Co spins initially aligned in the direction opposite to H_c (Fig. 1c). A further increase in H_c leads to an abrupt jump with a weak hysteretic behavior at $H_{flop} = 2.8$ T, which indicates a first-order spin-flop transition[30–33]. The characteristic of this transition can be identified by extrapolation of the linear slope above H_{flop} that crosses at the origin. Additional canting of the flop state above H_{flop} leads to the spin-flip state being reached at ~4.8 T. The schematics in Fig. 1d illustrate the AFM, spin-flop, and spin-flip states. As T rises, the H_{flop} in the M_c curve continuously moves toward lower H_c with a gradual reduction of the step-like feature (Supplementary Figs. S1 and S2). The H_{flop} at 300 K occurs at 0.8 T (Fig. 1c), and the measured M_c at 300 K still increases after transformation to the flipped state at ~2 T. This remaining slope is attributed to the thermal fluctuation, which interferes with the saturation of M_c. In contrast, M_{ab} at 2 K monotonically increases due to the steady canting of Fe/Co spins to the H_{ab} orientation, followed by a slope change at ~7 T (Fig. 1e). A slight hysteresis is observed in M_{ab}, which is attributed to the inhomogeneous distribution of Fe/Co atoms, previously confirmed by electron energy loss spectroscopy[34] (see Supplementary S1 for details). The overall magnitude of M_{ab} is reduced and the position of the change in the slope is lowered at 300 K. The crossing behavior, in which the value of M_c exceeds that of M_{ab} at H_{flop}, suggests a substantial modification of the anisotropic properties through H_{flop}.

The crucial aspects of the spin-flop transition were theoretically examined by employing a uniaxial anisotropic spin Hamiltonian (see "Methods" for details)[35]. To fit the theoretical results to the M_c observed at 2 K, we traced the global minimum of the total magnetic energy upon increasing H_c, obtaining the following relations: $g\mu_B H_{flop} S/JS^2 = 1.75$ and $JS^2 = 11.10 \times 10^5$ J/m^3, where JS^2 and $g\mu_B HS$ denote the exchange coupling and Zeeman energies, respectively. By fitting to the measured M_{ab}, we also obtained the ratio between the magnetocrystalline anisotropy constant K and JS^2, i.e., $K/JS^2 = 0.36$, and $K = 3.84 \times 10^5$ J/m^3. The presence of K, which tends to bind the spin orientations to the c-axis, stabilizes the AFM phase in zero H. The weak K regime (i.e., $K < JS^2$) enables the occurrence of the spin-flop transition at a sufficient magnitude of H along the magnetically easy c-axis. The resulting M_c and M_{ab} at 2 K, which are displayed in Fig. 1d, f, reproduce the anisotropic magnetic properties experimentally observed.

As the anisotropic magnetic properties at 300 K are significantly influenced by thermal fluctuations, the spin model was precisely analyzed by using a statistical approach at finite T. The spin S_i within a ferromagnetic Co/Fe layer was altered to $S_i(T,H)$ at a given T and H as $S_i(T,H) = S_i(T,0) + a(S_i(0,0) - S_i(T,0))H + b(S_i(0,0) - S_i(T,0))H^2$, where

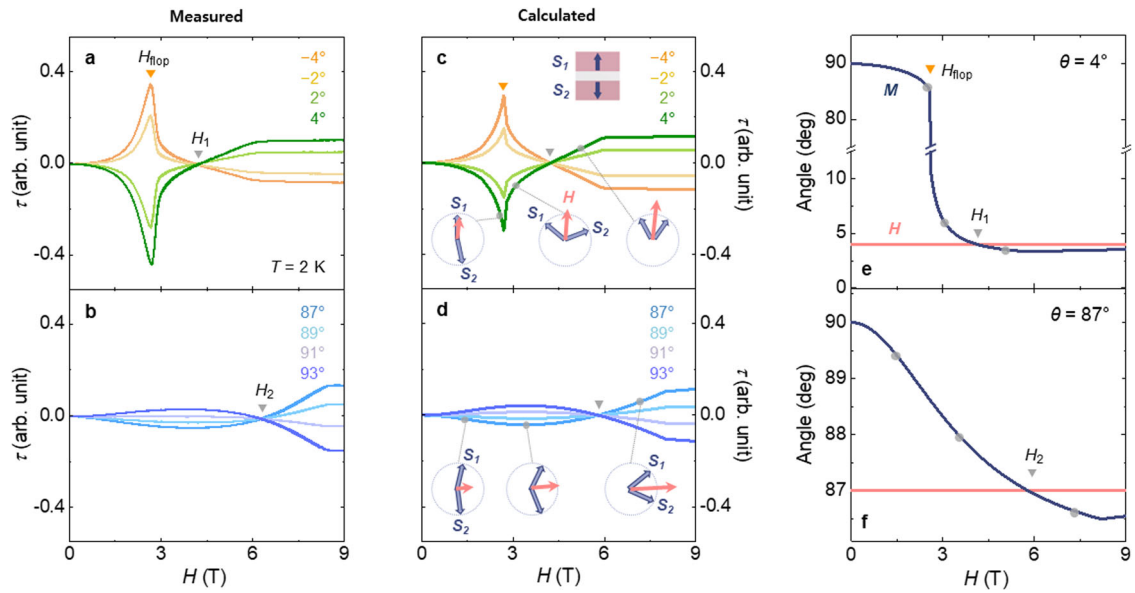

Fig. 2 Anisotropic magnetic torques at 2 K. a H dependence of the magnetic torque, τ, measured at $\theta = -4$, -2, 2, and 4° for $T = 2$ K. The orange and gray inverted triangles represent the occurrence of spin flops at H_{flop} and the crossing of the zero τ value at H_1, respectively. **b** H dependence of τ measured at $\theta = 87$, 89, 91, and 93° for $T = 2$ K. The gray inverted triangle indicates the crossing of the zero τ value at H_2. **c** Calculated H-dependent τ for $\theta = -4$, -2, 2, and 4°. The schematics illustrate the angle variation of the magnetic moments as H is increased at $\theta = 4°$. **d** Calculated H-dependent τ for $\theta = 87$, 89, 91, and 93°. The schematics illustrate the angle variation of the magnetic moments as H is increased at $\theta = 87°$. **e** Angular change in the net magnetization upon increasing H at $\theta = 4°$. **f** Angular change in the net magnetization upon increasing H at $\theta = 87°$.

the coefficients are $a = 5.0 \times 10^{-3}\,\mathrm{T}^{-1}$ and $b = 8.9 \times 10^{-3}\,\mathrm{T}^{-2}$ for $T = 300$ K, $S_i(0,0) = 4.76\,\mu_B$, and $S_i(300\mathrm{K},0) = 2.30\,\mu_B$. Considering a quasi-one-dimensional system, the effective T is given by $T_{eff} = T/N_c(T)$, where $N_c(T)$ is the average number of ferromagnetic spin clusters within a layer at a finite T. When T approaches zero, $N_c(T)$ approaches one since the spins are completely aligned. The isothermal M was averaged out using the following formula: $M(H) = \frac{1}{Z}\mathrm{Tr}[M(H)e^{-\tilde{\mathcal{H}}/k_B T_{\mathrm{eff}}}]$, where Z is the partition function, k_B is the Boltzmann constant, $\tilde{\mathcal{H}} \equiv \mathcal{H}/N$, and $M(H) = \hat{H} \cdot \sum_{i=1}^{2} \vec{S}_i(T,H)$. Our approach results in moderate coincidence with the experimental M_c and M_{ab} data at 300 K (Fig. 1d, f) and provides the relationship $g\mu_B H_{\mathrm{flop}} S/JS^2 = 1.08$ with $JS^2 = 3.10 \times 10^5\,\mathrm{J/m^3}$. In addition, the ratio $K/JS^2 = 0.16$ is still sufficient to result in the spin-flop transition at room T, despite the large reduction of JS^2.

Magnetic-field-dependent magnetic torques

Measuring the magnetic torque per unit volume, $\tau = \boldsymbol{M} \times \boldsymbol{H}$, provides an alternative approach to examine the anisotropic magnetic properties and occurrence of spin flops, as shown in Fig. 2. An FCGT crystal with a size of $0.20 \times 0.15 \times 0.05\,\mathrm{m}^3$ was used for the τ measurement. The reproducibility of the τ measurement was tested with several different pieces of crystals from the same batch (Supplementary Fig. S3). H deviates from the c-axis by an angle θ ($\theta = 0°$ for the H_c direction and $\theta = 90°$ for the H_{ab} direction). At $\theta = 0°$, the value of τ is zero due to the parallel or antiparallel alignment between the magnetic moments in a certain layer and H_c below H_{flop}. Furthermore, the values of τ in the spin-flop state formed above H_{flop} cancel out due to the equal magnitudes but opposite signs of τ (see the schematic in Fig. 1d). The value of τ is also zero at $\theta = 90°$ because the same amount of gradual canting of magnetic moments in adjacent layers at H_{ab} leads to a null τ. Therefore, anisotropic signals of τ were observed at θ close to 0 and 90°. At $T = 2$ K and $\theta = -2°$, $\tau(H)$ starts from zero and sharply increases as H is increased, showing a peak at H_{flop} (Fig. 2a). Beyond H_{flop}, τ continually decreases and changes to negative values by crossing zero at $H_1 \approx 4.2$ T. At $\theta = -4°$, the larger deviation from 0° produces an enhanced peak at H_{flop}. At $\theta = 2$ and 4°, τ is fully reversed due to its sign change from the formation of the opposite angle between the net M and H. For θ close to 90°, τ exhibits a small and broad variation with increasing H, and its sign change occurs at $H_2 \approx 6.3$ T (Fig. 2b). The evident difference in the behavior of τ is attributed to the strongly anisotropic nature of FCGT crystals. The T dependence of magnetic τ at various H values and $\theta = -4°$ is shown in Supplementary Fig. S4.

The merit of our spin-model calculation is obvious in the direct quantification of the net moment orientation in each layer relative to H (schematics in Fig. 2c, d), which reproduces the anisotropic $\tau(H)$ near 0° and 90°, as plotted in Fig. 2c, d. Under H below H_{flop} for $\theta = 4°$, the dominant H_c component tends to maintain the direction of the net

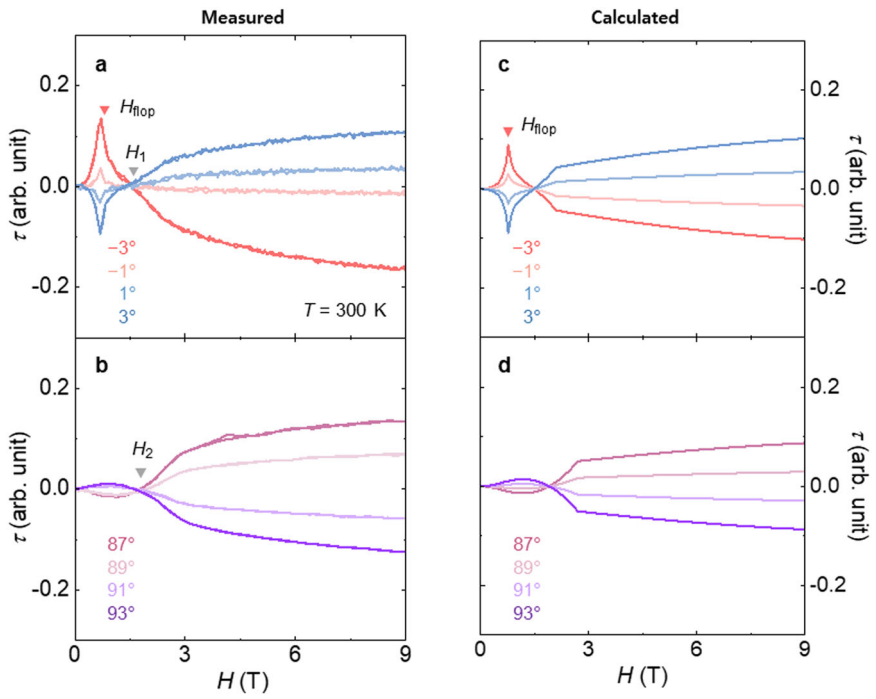

Fig. 3 Anisotropic magnetic torques at room temperature. **a** H dependence of the magnetic torque, τ, measured at $\theta = -3$, -1, 1, and 3° for $T = 300$ K. The red and gray inverted triangles indicate the occurrence of spin flops at H_{flop} and crossing of the zero τ value at H_1, respectively. **b** H dependence of τ measured at $\theta = 87$, 89, 91, and 93° for $T = 300$ K. The gray inverted triangle denotes the crossing of the zero τ value at H_2. **c** Calculated H-dependent τ for $\theta = -3$, -1, 1, and 3°. **d** Calculated H-dependent τ for $\theta = 87$, 89, 91, and 93°.

moment in the upper layer ($\boldsymbol{S_1}$ moment shown in the inset of Fig. 2c) close to 0°, and the slight H_{ab} component affects the net moment in the lower layer ($\boldsymbol{S_2}$ moment). Accordingly, the $\boldsymbol{S_2}$ moment is canted greater than the $\boldsymbol{S_1}$ moment (Fig. 2c). Thus, the net M (i.e., the sum of $\boldsymbol{S_1}$ and $\boldsymbol{S_2}$ moments) points to an angle below 90° (Fig. 2e), generating negative τ values. For the spin-flop state formed beyond H_{flop}, the angle of the net M is still larger than $\theta = 4°$ (Fig. 2e), whereas the negative τ value is maintained because the $\boldsymbol{S_2}$ moment is canted further due to the influence of the H_{ab} component. However, both the $\boldsymbol{S_1}$ and $\boldsymbol{S_2}$ moments at high H above H_1 tend to align close to the H_c direction and are less affected by the small H_{ab} component. The resulting net M turns to slightly less than $\theta = 4°$ (Fig. 2e), followed by sign reversal of τ (Fig. 2c). At $\theta = 87°$, the less rotated $\boldsymbol{S_2}$ moment engenders an angle of the net M larger than θ and negative τ values (Fig. 2d, f). Under the high H above H_2, the larger H_c component rotates the $\boldsymbol{S_1}$ moment further to a smaller θ orientation. Simultaneously, the angle of the net M becomes smaller than $\theta = 87°$, and the sign of τ changes to positive values.

At room T, the peak indicating H_{flop} is well maintained (Fig. 3a). At θ near 90°, broad variations in τ are also observed when sweeping H (Fig. 3b). Sign reversal of τ occurs at $H_1 \approx 1.6$ T near $\theta = 0°$ and at $H_2 \approx 1.7$ T near $\theta = 90°$. The precise trace of the minimum total magnetic energy for the spin Hamiltonian generates the orientation of the magnetic moment in each layer. The resulting τ values obtained by sweeping H coincide with the experimental results (Fig. 3a, c and Fig. 3b, d).

Direct connection between spin states and magnetic torque data at room temperature

The angle dependence of the magnetic τ reveals the details of the evolving anisotropic magnetic properties through the spin-flop transition at room T ($T = 300$ K), as plotted in Fig. 4. The geometry of the τ measurement is depicted in the schematic of Fig. 4a, in which H with an angle θ from the c-axis is rotated. In the spin-flop regime ($H = 0.7$ T), asymmetric angular-dependent τ values are observed (Fig. 4b). The slopes of τ near $\theta = 0$ and 180° appear to be larger than those at $\theta = 90$ and 270°, which originate from the peak feature of $\tau(H)$ at the spin-flop transition observed near $\theta = 0°$ (Fig. 3a). The larger magnitude of τ near $\theta = 0$ and 180° is well displayed in the 3D H–θ contour plot of Fig. 4c. At $H = 1.6$ T, τ near $\theta = 0$ and 180° shows a plateau-like behavior with zero τ when $\tau(H)$ changes to negative values by crossing zero at H_1. Under a slightly increased H ($H = 1.7$ T), the values of τ near $\theta = 0$ and 180° are partly reversed due to the negative values of $\tau(H)$ above H_1. The sign of τ is completely reversed at $H = 3$ T, which is considerably higher than

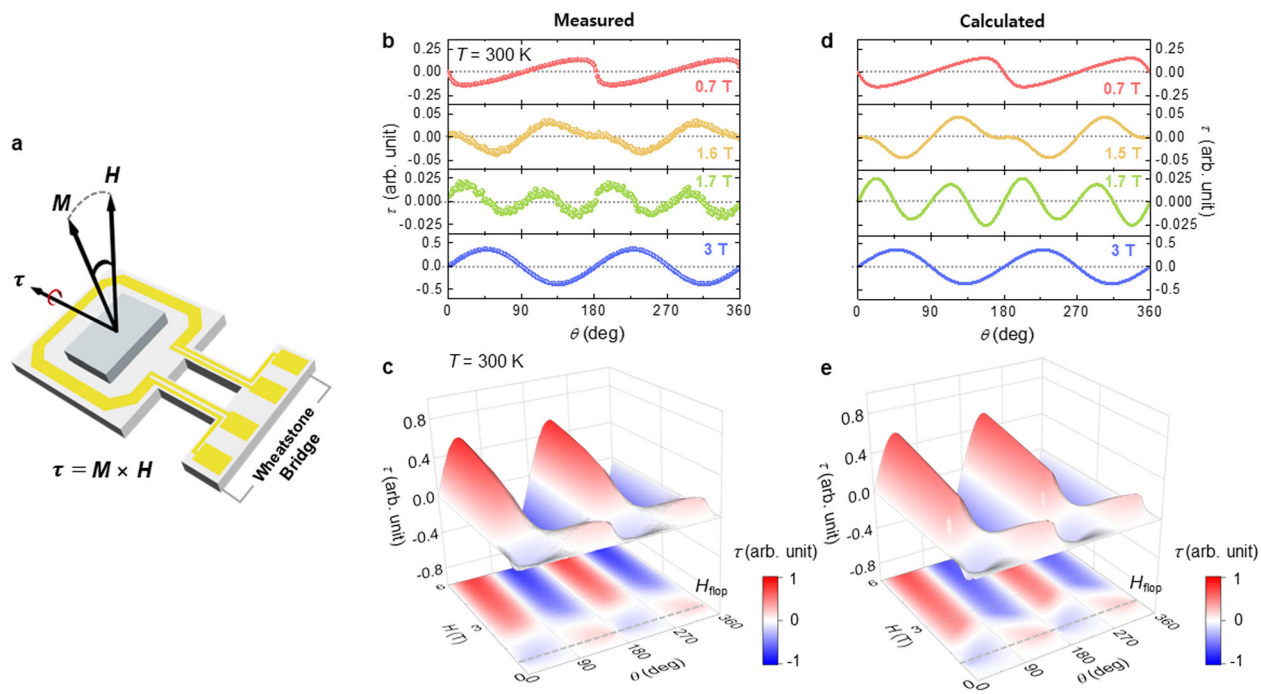

Fig. 4 Measured and calculated magnetic torques at room temperature. a Schematic of the magnetic torque measurement using a piezoresistive cantilever connected to a Wheatstone bridge circuit. H deviating from the c-axis by the angle θ is rotated. **b** Angle dependence of the magnetic torque per unit volume, $\tau = \boldsymbol{M} \times \boldsymbol{H}$, measured at $T = 300$ K and $H = 0.7$, 1.6, 1.7, and 3 T. The scale of τ at 9 T is ten and twenty times larger than the scales at 1.6 and 1.7 T, respectively. **c** 3D contour plot of the angle-dependent τ data measured at different H and $T = 300$ K. **d** Angle dependence of τ estimated from the uniaxial anisotropic spin model at $H = 0.7$, 1.5, 1.7, and 3 T. **e** 3D contour plot constructed from the angle-dependent τ data calculated at different H.

H_{flop}, due to the sign change of $\tau(H)$ across H_2 near $\theta = 90$ and 270°. In the H–θ contour plot, two distinct aspects can be clearly identified: an asymmetric and large variation in τ at H_{flop} and H-driven reversal of τ above H_{flop} (Fig. 4c). In our theoretical estimation of the angle-dependent τ, the minimum of the total magnetic energy regarding the Hamiltonian model was calculated during the rotation of a specific H, which generates the value of τ associated with the orientation of the magnetic moment in each layer at a given angle. A τ variation trend similar to that in the experiments is observed as H increases (Fig. 4d), suggesting that the anisotropic spin model with a sizable magnetocrystalline anisotropy can explain the evolution of the anisotropic properties through the magnetic transition. As plotted in Fig. 4e, the estimated H–θ contour plot is also compatible with the experimental results. The T development of angle-dependent τ is described in Supplementary Figs. S5 and S6.

The approach using the easy-axis spin model enables us to build particular net moment orientations during the rotation of H. The outcome explains the connection between distinct spin states and the magnetic τ data at room T. As a weak $H = 0.5$ T is rotated from 0 to 45°, the two net moments of both layers are only slightly tilted due to the sizable magnetocrystalline anisotropy, which tends to preferentially orientate the spins to the magnetic easy c-axis (Fig. 5a). As a result, a small negative τ value is obtained for the configuration of the $\boldsymbol{S_1}$ moment close to the H direction. At $\theta = 90°$, τ crosses the zero value with equal and small canting angles of the net moments toward H_{ab}. Further rotation of H to $\theta = 135°$ changes τ to positive values with the canted arrangement in which the $\boldsymbol{S_2}$ moment is located adjacent to H. Similar sign variations are repeated, leading to a periodic angle dependence (Fig. 4b). At $H = 1.5$ T, the spin-flop state, in which the net moments are symmetrically arranged around H, is maintained in the low θ regime, exhibiting plateau-like behavior (Fig. 5b). With further rotation of H, the orientation of the $\boldsymbol{S_1}$ moment becomes adjacent to the H direction, with negative τ values. The τ state varies from negative to positive values by crossing $\theta = 90°$ and the $\boldsymbol{S_2}$ moment aligning close to the H direction. The spin states with the rotation of $H = 1.7$ T above H_{flop}, shown in Fig. 5c, provide a detailed explanation of the partly reversed behavior of τ near $\theta = 0$ and 180°. The spin-flop state at $\theta = 0°$ transforms to another tilted configuration that brings the $\boldsymbol{S_2}$ moment close to the H direction and generates a positive value of τ at $\theta = 22.5°$. With additional rotation of H, the τ state converts from positive to negative by crossing zero at $\theta = 45°$. The negative τ value

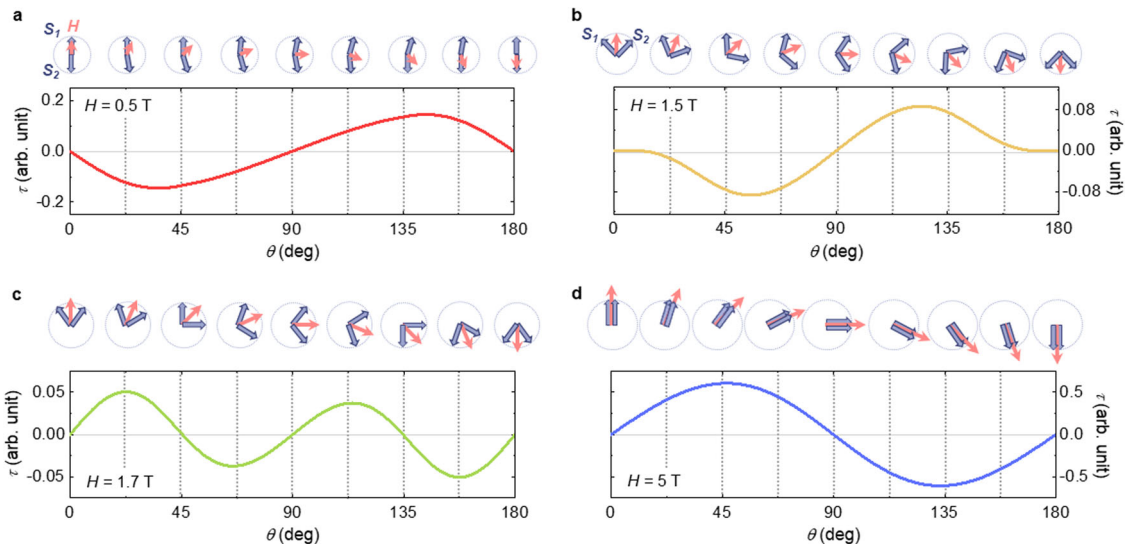

Fig. 5 Direct connection between spin states and angle-dependent torques at room temperature. a Angular dependence of magnetic τ calculated by fitting to the experimental τ data at $T = 300$ K. H is rotated in the *ac* plane with $H = 0.5$ T. The schematics depict the configurations of the net magnetic moments in the upper ($\boldsymbol{S_1}$) and lower ($\boldsymbol{S_2}$) layers with respect to the H direction. **b**, **c**, and **d** Calculated angle-dependent τ and corresponding net moment orientations at $H = 1.5$, 1.7, and 5 T, respectively.

at $\theta = 67.5°$ corresponds to the orientation of the $\boldsymbol{S_1}$ moment being adjacent to the H direction. In this way, τ shows a small magnitude but changes its sign twice as much for the fully rotating H. In a strong field $H = 5$ T, which is sufficient to saturate the net moments of both orientations, $\theta = 0$ and 90°, the overall angular dependence of τ is entirely reversed, with an increased magnitude of τ (Fig. 5d). The net moments in the two layers exhibit a collective motion induced by the rotation of H. However, the orientations of the moments relative to H are still influenced by magnetocrystalline anisotropy. For $\theta < 90°$, H, which incorporates a positive c component, turns the net moments closer to the positive c-axis and yields a positive τ value. At $\theta > 90°$, the net moments are rotated more than H, resulting in a negative τ state.

Discussion

Unlike conventional methods, such as vibrating sample magnetometry, the magnetic torque measurement method has been developed to adequately observe the angular dependence of magnetic properties and detect tiny torque variations with extreme sensitivity[36]. Thus, it seems appropriate for examining vdW magnets with highly anisotropic magnetic properties inherently implicated by their 2D nature[37–39]. A certain axial or planar magnetic anisotropy incorporated in an antiferromagnet strongly affects the relative angle deviation between the spin and magnetic field orientations, which leads to a certain value of the magnetic torque. However, ordinary phenomenological analyses were mostly performed by simple fitting using a series of sinusoidal functions derived from the angle dependence of the magnetic free energy[22,40,41]. As such, the interpretations were limited due to the difficulty in identifying the strength of the magnetocrystalline anisotropy and configurations of relevant spin states. Moreover, the verification of the magnetic torque variations in the magnetic phase transitions remains restricted[42]. In the high-T_N vdW antiferromagnet FCGT, we quantified the magnetocrystalline anisotropy energy and determined specific spin states formed during the rotation of H, which were intimately correlated with the progressive reversal feature of the angle-dependent magnetic torque. Experimental techniques such as neutron diffraction and resonant X-ray scattering, which necessarily require large facilities, are generally selected to verify the microscopic spin structures of diverse antiferromagnets[22,43–45]. However, the detection of these continuously variable spin states in the presence of rotating magnetic fields is technically challenging owing to the limiting field geometry. In this regard, a recognizable benefit of our advanced theoretical approaches consists of the convenient access to the spin orientations in each layer through the estimation of the minimum magnetic energy with respect to the uniaxial anisotropic spin Hamiltonian. Furthermore, the flexibility of the anisotropic spin Hamiltonian approach has broad applicability to other types of antiferromagnetic materials.

Acknowledgements

This work was supported by the National Research Foundation of Korea (NRF) through grants 2016R1D1A1B01013756, NRF-2017R1A5A1014862 (SRC program: vdWMRC center), NRF-2021R1A2C1006375, and NRF-2022R1A2C1006740. We would like to thank Editage (www.editage.co.kr) for English language editing.

Author contributions
M.K.K., N.L., and Y.J.C. initiated and supervised the project. H.J.S. and J.S.K. synthesized the single crystals. H.J.S., J.S.K., J.H.K., J.Y.S., J.M.H., and K.W.J. performed measurements of the physical properties. M.K.K. and K.M. performed the theoretical calculations. H.J.S., J.S.K., M.K.K., K.M., N.L., and Y.J.C. analyzed the data and prepared the manuscript. All authors have read and approved the final version of the manuscript.

Conflict of interest
The authors declare no competing interests.

Publisher's note
Springer Nature remains neutral with regard to jurisdictional claims in published maps and institutional affiliations.

Supplementary information The online version contains supplementary material available at https://doi.org/10.1038/s41427-023-00467-y.

Received: 29 October 2022 Revised: 26 January 2023 Accepted: 31 January 2023.
Published online: 3 March 2023

References
1. Novoselov, K. S. et al. Two-dimensional atomic crystals. *Proc. Natl Acad. Sci. USA* **102**, 10451–10453 (2005).
2. Burch, K. S., Mandrus, D. & Park, J.-G. Magnetism in two-dimensional van der Waals materials. *Nature* **563**, 47–52 (2018).
3. Gibertini, M., Koperski, M., Morpurgo, A. F. & Novoselov, K. S. Magnetic 2D materials and heterostructures. *Nat. Nanotechnol.* **14**, 408–419 (2019).
4. Liu, Y. et al. Van der Waals heterostructures and devices. *Nat. Rev. Mater.* **1**, 16042 (2016).
5. Mak, K. F., Shan, J. & Ralph, D. C. Probing and controlling magnetic states in 2D layered magnetic materials. *Nat. Rev. Phys.* **1**, 646–661 (2019).
6. Gong, C. & Zhang, X. Two-dimensional magnetic crystals and emergent heterostructure devices. *Science* **363**, eaav4450 (2019).
7. Novoselov, K. S., Mishchenko, A., Carvalho, A. & Castro Neto, A. H. 2D materials and van der Waals heterostructures. *Science* **353**, aac9439 (2016).
8. Sierra, J. F., Fabian, J., Kawakami, R. K., Roche, S. & Valenzuela, S. O. Van der Waals heterostructures for spintronics and opto-spintronics. *Nat. Nanotechnol.* **16**, 856–868 (2021).
9. Mermin, N. D. & Wagner, H. Absence of ferromagnetism or antiferromagnetism in one- or two-dimensional isotropic Heisenberg models. *Phys. Rev. Lett.* **17**, 1133–1136 (1966).
10. Gong, C. et al. Discovery of intrinsic ferromagnetism in two-dimensional van der Waals crystals. *Nature* **546**, 265–269 (2017).
11. Huang, B. et al. Layer-dependent ferromagnetism in a van der Waals crystal down to the monolayer limit. *Nature* **546**, 270–273 (2017).
12. Fei, Z. et al. Two-dimensional itinerant ferromagnetism in atomically thin Fe_3GeTe_2. *Nat. Mater.* **17**, 778–782 (2018).
13. Deng, Y. et al. Gate-tunable room-temperature ferromagnetism in two-dimensional Fe_3GeTe_2. *Nature* **563**, 94–99 (2018).
14. Lee, J.-U. et al. Ising-type magnetic ordering in atomically thin $FePS_3$. *Nano Lett.* **16**, 7433–7438 (2016).
15. Lado, J. L. & Fernández-Rossier, J. On the origin of magnetic anisotropy in two dimensional CrI_3. *2D Mater.* **4**, 035002 (2017).
16. McGuire, M. A., Dixit, H., Cooper, V. R. & Sales, B. C. Coupling of crystal structure and magnetism in the layered, ferromagnetic insulator CrI_3. *Chem. Mater.* **27**, 612–620 (2015).
17. Zhang, H. et al. Itinerant ferromagnetism in van der Waals $Fe_{5-x}GeTe_2$ crystals above room temperature. *Phys. Rev. B* **102**, 064417 (2020).
18. Seo, J. et al. Tunable high-temperature itinerant antiferromagnetism in a van der Waals magnet. *Nat. Commun.* **12**, 2844 (2021).
19. Néel, L. Magnetic properties of the metallic state and interaction energy between magnetic atoms. *Ann. Phys.* **11**, 232–279 (1936).
20. Nagamiya, T., Yosida, K. & Kubo, R. Antiferromagnetism. *Adv. Phys.* **4**, 1–112 (1955).
21. Gorter, C. J. Observations on antiferromagnetic $CuCl_2{\cdot}H_2O$ crystals. *Rev. Mod. Phys.* **25**, 332–337 (1953).
22. Peng, Y. et al. Magnetic structure and metamagnetic transitions in the van der Waals antiferromagnet $CrPS_4$. *Adv. Mater.* **32**, 2001200 (2020).
23. Wang, Z. et al. Determining the phase diagram of atomically thin layered antiferromagnet $CrCl_3$. *Nat. Nanotechnol.* **14**, 1116–1122 (2019).
24. Long, G. et al. Persistence of magnetism in atomically thin $MnPS_3$ crystals. *Nano Lett.* **20**, 2452–2459 (2020).
25. Huang, B. et al. Electrical control of 2D magnetism in bilayer CrI_3. *Nat. Nanotechnol.* **13**, 544–548 (2018).
26. May, A. F. et al. Ferromagnetism near room temperature in the cleavable van der Waals crystal Fe_5GeTe_2. *ACS Nano* **13**, 4436–4442 (2019).
27. May, A. F., Du, M.-H., Cooper, V. R. & McGuire, M. A. Tuning magnetic order in the van der Waals metal Fe_5GeTe_2 by cobalt substitution. *Phys. Rev. Mater.* **4**, 074008 (2020).
28. Tian, C. et al. Tunable magnetic properties in van der Waals crystals $(Fe_{1-x}Co_x)_5GeTe_2$. *Appl. Phys. Lett.* **116**, 202402 (2020).
29. Zhang, H. et al. Room-temperature skyrmion lattice in a layered magnet $(Fe_{0.5}Co_{0.5})_5GeTe_2$. *Sci. Adv.* **8**, eabm7103 (2022).
30. Machado, F. L. A. et al. Spin-flop transition in the easy-plane antiferromagnet nickel oxide. *Phys. Rev. B* **95**, 104418 (2017).
31. Ouyang, Z. W., Pecharsky, V. K., Gschneidner, K. A., Schlagel, D. L. & Lograsso, T. A. Angular dependence of the spin-flop transition and a possible structure of the spin-flop phase of Gd_5Ge_4. *Phys. Rev. B* **76**, 134415 (2007).
32. Sass, P. M., Kim, J., Vanderbilt, D., Yan, J. & Wu, W. Robust *A*-type order and spin-flop transition on the surface of the antiferromagnetic topological insulator $MnBi_2Te_4$. *Phys. Rev. Lett.* **125**, 037201 (2020).
33. Zhu, F. et al. Magnetic structures, spin-flop transition, and coupling of Eu and Mn magnetism in the Dirac semimetal $EuMnBi_2$. *Phys. Rev. Res.* **2**, 043100 (2020).
34. Zhang, H. et al. A room temperature polar magnetic metal. *Phys. Rev. Mater.* **6**, 044403 (2022).
35. Berkowitz, A. E. & Takano, K. Exchange anisotropy—a review. *J. Magn. Magn. Mater.* **200**, 552–570 (1999).
36. Losby, J. E., Sauer, V. T. K. & Freeman, M. R. Recent advances in mechanical torque studies of small-scale magnetism. *J. Phys. D: Appl. Phys.* **51**, 483001 (2018).
37. Zhang, T. et al. Magnetism and optical anisotropy in van der Waals antiferromagnetic insulator CrOCl. *ACS Nano* **13**, 11353–11362 (2019).
38. Afanasiev, D. et al. Controlling the anisotropy of a van der Waals antiferromagnet with light. *Sci. Adv.* **7**, eabf3096 (2021).
39. Xiao, F. & Tong, Q. Tunable strong magnetic anisotropy in two-dimensional van der Waals antiferromagnets. *Nano Lett.* **22**, 3946–3952 (2022).
40. Modic, K. A. et al. Robust spin correlations at high magnetic fields in the harmonic honeycomb iridates. *Nat. Commun.* **8**, 180 (2017).
41. Riedl, K., Li, Y., Winter, S. M. & Valentí, R. Sawtooth torque in anisotropic j_{eff}=1/2 magnets: application to α-$RuCl_3$. *Phys. Rev. Lett.* **122**, 197202 (2019).
42. Nauman, M. et al. Complete mapping of magnetic anisotropy for prototype Ising van der Waals $FePS_3$. *2D Mater.* **8**, 035011 (2021).
43. McGuire, M. A. et al. Antiferromagnetism in the van der Waals layered spin-lozenge semiconductor $CrTe_3$. *Phys. Rev. B* **95**, 144421 (2017).
44. Nawa, K. et al. Magnetic structure study of the sawtooth chain antiferromagnet $Fe_2Se_2O_7$. *Sci. Rep.* **11**, 24049 (2021).
45. Biniskos, N. et al. Complex magnetic structure and spin waves of the non-collinear antiferromagnet Mn_5Si_3. *Phys. Rev. B* **105**, 104404 (2022).